RESEARCH ARTICLE | JULY 09 2024

Cubic Mn_3Ge thin films stabilized through epitaxial growth as a candidate noncollinear antiferromagnet

Special Collection: Topological and Chiral Matter – Physics and Applications

Anastasios Markou ; James M. Taylor ; Jacob Gayles ; Yan Sun ; Dominik Kriegner ; Joerg Grenzer; Shanshan Guo ; Walter Schnelle ; Edouard Lesne ; Claudia Felser ; Stuart S. P. Parkin

Appl. Phys. Lett. 125, 022402 (2024)
https://doi.org/10.1063/5.0206194

Applied Physics Letters ARTICLE pubs.aip.org/aip/apl

Cubic Mn_3Ge thin films stabilized through epitaxial growth as a candidate noncollinear antiferromagnet

Cite as: Appl. Phys. Lett. **125**, 022402 (2024); doi: 10.1063/5.0206194
Submitted: 29 February 2024 · Accepted: 17 June 2024 ·
Published Online: 9 July 2024

View Online Export Citation CrossMark

Anastasios Markou,[1,2,a)] James M. Taylor,[3,4,a)] Jacob Gayles,[5] Yan Sun,[6] Dominik Kriegner,[7] Joerg Grenzer,[8] Shanshan Guo,[1] Walter Schnelle,[1] Edouard Lesne,[1] Claudia Felser,[1] and Stuart S. P. Parkin[3,a)]

AFFILIATIONS

[1]Department of Topological Quantum Chemistry, Max Planck Institute for Chemical Physics of Solids, 01187 Dresden, Germany
[2]Department of Physics, University of Ioannina, 45110 Ioannina, Greece
[3]NISE Department, Max Planck Institute of Microstructure Physics, 06120 Halle, Germany
[4]Institute of Physics, Martin Luther University Halle-Wittenberg, 06120 Halle, Germany
[5]Department of Physics, University of South Florida, Tampa, Florida 33620, USA
[6]Institute of Metal Research, Shenyang National Laboratory for Materials Science, Chinese Academy of Sciences, Shenyang 110016, China
[7]Institute of Physics, Czech Academy of Sciences, 16253 Praha 6, Czech Republic
[8]Institute of Radiation Physics, Helmholtz-Zentrum Dresden-Rossendorf, 01328 Dresden, Germany

Note: This paper is part of the APL Special Collection on Topological and Chiral Matter—Physics and Applications.
[a)]**Authors to whom correspondence should be addressed:** amarkou@uoi.gr; james.taylor@physik.uni-halle.de; and stuart.parkin@mpi-halle.mpg.de

ABSTRACT

Metallic antiferromagnets with chiral spin textures induce Berry curvature-driven anomalous and spin Hall effects that arise from the topological structure of their electronic bands. Here, we use epitaxial engineering to stabilize (111)-oriented thin films of Mn_3Ge with a cubic phase. This cubic phase is distinct from tetragonal ferrimagnetic and hexagonal noncollinear antiferromagnetic structures with the same chemical composition. First-principles calculations indicate that cubic Mn_3Ge will preferentially form an all-in/all-out triangular spin texture. We present evidence for this noncollinear antiferromagnetism through magnetization measurements with a Néel temperature of 490 K. First-principles calculations of the corresponding band structure indicate the presence of Weyl points. These highlight cubic Mn_3Ge as a candidate material for topological antiferromagnetic spintronics.

Topological spin-orbitronics is an emerging research field that utilizes the spin–orbit coupling (SOC) between conduction electrons and the lattice of crystalline materials to achieve functionalities relevant to devices.[1] These include Berry curvature-driven magnetotransport, such as the anomalous Hall effect (AHE)[2] and the spin Hall effect (SHE),[3] as well as topological magnetic textures.[4] The local crystal configuration governs the exchange interactions between magnetic atoms, leading to, for example, geometric frustration or antisymmetric exchange (Dzyaloshinskii–Moriya interaction, DMI). When combined, these can lead to chiral noncollinear antiferromagnetic (AF) spin textures.[5] These break time-reversal symmetry and thus, when further combined with large SOC, create band structure nodes that act as sources and sinks of Berry curvature.[6]

Mn_3Ge polymorphic compounds are of particular interest, because multiple phases have been observed, specifically tetragonal (*t*-) $D0_{22}$ (Ref. 7) and hexagonal (*h*-) $D0_{19}$ structures.[8] Both have the same atomic composition but exhibit very different magnetic phenomena. The tetragonal phase is a ferrimagnet with hard magnetic properties.[9]

However, the hexagonal phase has an in-plane triangular AF structure with negative vector chirality, from which a large Berry curvature sourced AHE arises.[10] This is achieved thanks to a small net in-plane moment allowing for external magnetic field orientation of the AF domains.[11] Additionally, when this hexagonal phase is coupled with a superconductor, proximity-induced long-range spin triplet supercurrents are observed.[12]

The Berry curvature-driven AHE was originally predicted for the cubic (c-) phase of Mn_3Ir,[13] which possesses a similar chiral spin texture to h-Mn_3Ge, albeit with positive vector chirality. However, the distinct magnetocrystalline anisotropy (MCA) of the cubic lattice excludes a net uncompensated moment, and, as such, magnetic fields cannot set the AF domains in one orientation. Rather there are equal numbers of domains, each of which have opposite "handedness" of spin texture chirality, with canceling contributions to AHE.[14] However, a sizable SHE was demonstrated experimentally in c-Mn_3Ir, because the spin Berry curvature from which it arises has the same sign in domains with opposite chiral senses of rotation.[15]

In this work, we combine these two flavors of noncollinear AF, to stabilize a Mn_3Ge phase with cubic crystal structure. Magnetization measurements show no evidence of a finite moment. However, when coupled to ferromagnetic (FM) Permalloy (Py, $Ni_{81}Fe_{29}$), the heterostructure exhibits a sizable exchange bias indicative of antiferromagnetic order in the c-Mn_3Ge film. Complementary first-principles electronic structure calculations suggest that this is a noncollinear all-in/all-out antiferromagnetic ordering, together with the presence of Weyl nodes.

The aforementioned cubic phase was stabilized through the epitaxial growth of Mn_3Ge thin films, in a similar process to that reported in our previous work.[16] 10-, 30-, and 40-nm-thick films were deposited on single-crystal (111)-cut $SrTiO_3$ (STO) substrates with a 5-nm-thick Ru buffer layer. The Ru underlayer was deposited at a temperature of 400 °C, with subsequent Mn and Ge co-deposition at room temperature, followed by a 400 °C annealing step. Finally, a 3-nm-thick Al film, which itself partially oxidizes, caps the epilayers.

The resulting stoichiometry was estimated to be $Mn_{75}Ge_{25}$ (±2 at. %) by energy dispersive x-ray spectroscopy (EDXS) and verified using inductively coupled plasma optical emission spectrometry. We further investigated the films' crystalline structure and morphology using a combination of x-ray diffraction (XRD), reciprocal space mapping (RSM), x-ray reflectivity (XRR), and atomic force microscopy (AFM). Details of these methods are given in the supplementary material.

Figure 1(a) depicts a symmetric θ-2θ XRD scan of a 40 nm Mn_3Ge film on a 5 nm Ru underlayer. We attribute the observed peaks to the {0001} and {111} reflections from Ru and Mn_3Ge, respectively. This is a first indication that h-Ru seeds the epitaxial growth of (111)-oriented c-Mn_3Ge. The fitted diffraction peak positions allow us to calculate an out-of-plane lattice spacing of $d_{111} = (2.16 \pm 0.02)$ Å for the c-Mn_3Ge phase. Assuming a cubic unit cell, this yields a lattice parameter of $a = (3.74 \pm 0.03)$ Å, which matches with that recently reported using Pt buffer layers on Si/SiO_2 substrates.[17]

Off-specular XRD scans [upper inset to Fig. 1(b)] reveal the asymmetric (201) Bragg reflection of the c-Mn_3Ge layer, suggesting a high degree of chemical ordering consistent with an $L1_2$-type structure. This is similar to high-pressure synthesized cubic $L1_2$-Mn_3Ge bulk crystals[18] and in contrast to disordered γ-type Mn_3Ge films reported in Ref. 17.

To confirm this cubic-type crystal structure, we measure RSM at two different azimuthal angles. Figure 1(c) shows the reciprocal-space

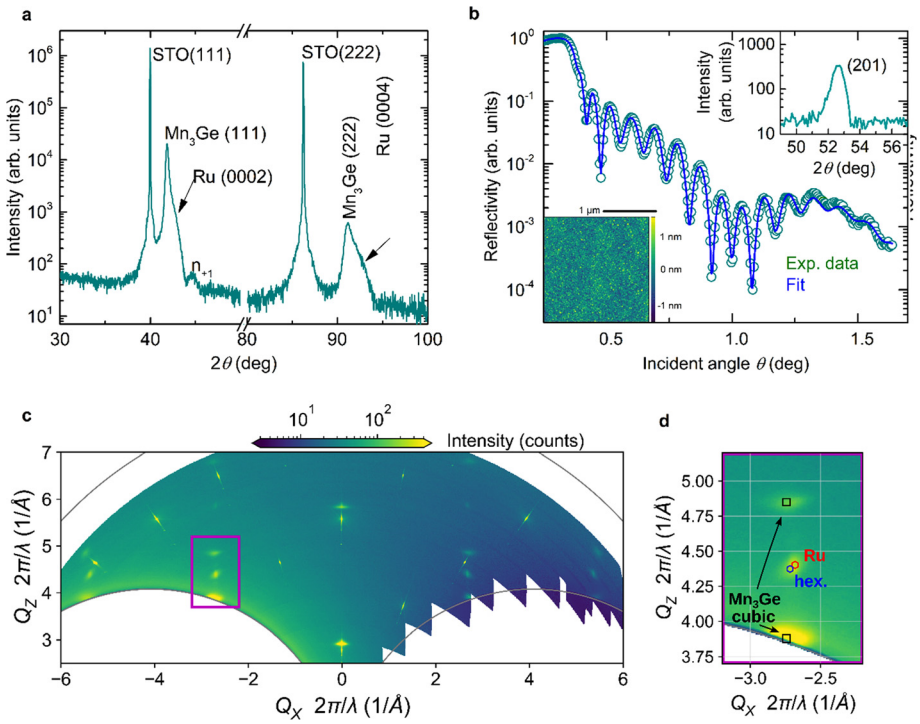

FIG. 1. Structural and morphological properties of a STO (111)/Ru (5 nm)/Mn_3Ge (40 nm) sample. (a) Symmetric XRD scan. (b) XRR pattern. Lower and upper insets show, respectively, the AFM topography and the asymmetric (201) XRD peak. (c) RSM measured with the [11$\bar{2}$] and [111] directions of the substrate as the x and y axis. The marked region is enlarged in (d). Nominal positions of Bragg peaks from the h-Ru (red hexagon) buffer layer, as well as from the h-Mn_3Ge (blue hexagon) and c-Mn_3Ge (black squares) candidate crystal structures are indicated.

plane containing the substrate [11$\bar{2}$] (x axis) and [111] (y axis) directions, while supplementary material Fig. S1 shows the orthogonal plane. A zoomed-in view, Fig. 1(d), demonstrates Bragg peaks best fitted by *h*-Ru- and *c*-Mn_3Ge-type structures. For comparison, we mark the expected positions of the Bragg peaks from the hexagonal $P6_3/mmc$ Mn_3Ge structure to demonstrate that the precise positions of the observed peaks are consistent only with the cubic variant.

From the fitted peak positions, we analyze the precise unit cell shape. We find a unit cell angle of $\alpha = (90.3 \pm 0.2)^\circ$, indicating a slight rhombohedral distortion away from a perfect cubic unit cell. Such small rhombohedral distortions are commonly found in thin films with in-plane lattice mismatch, explained in our case by the ∼2% larger lattice spacing in the Ru buffer. In addition, our numerical analysis yields a lattice parameter of $a = (3.76 \pm 0.02)$ Å. This agrees to within error with the lattice parameter calculated using the d_{111} spacing from specular XRD scans.

In order to investigate the crystal structure locally, we performed cross-sectional transmission electron microscopy (TEM), high-resolution TEM (HRTEM), and scanning TEM (STEM) with the high-angle annular dark-field technique (HAADF-STEM) while using a built-in EDXS detector for element mapping. Technical details are given in the supplementary material. Figure 2(a) depicts HRTEM of a STO (111)/Ru (10 nm)/Mn_3Ge (30 nm) sample. This demonstrates the single crystalline nature of the Mn_3Ge film. Fast Fourier transform (FFT) diffractograms are taken from two different regions of the Mn_3Ge layer. The upper FFT diffractogram shows reflections corresponding to the {111} and {200} family of planes. Their positions are consistent with a (111)-oriented cubic structure-type. In the lower FFT, we observe supplementary diffraction spots (in addition to those from the main structure, marked by yellow circles), which demonstrate local rotational twining parallel to the substrate plane.

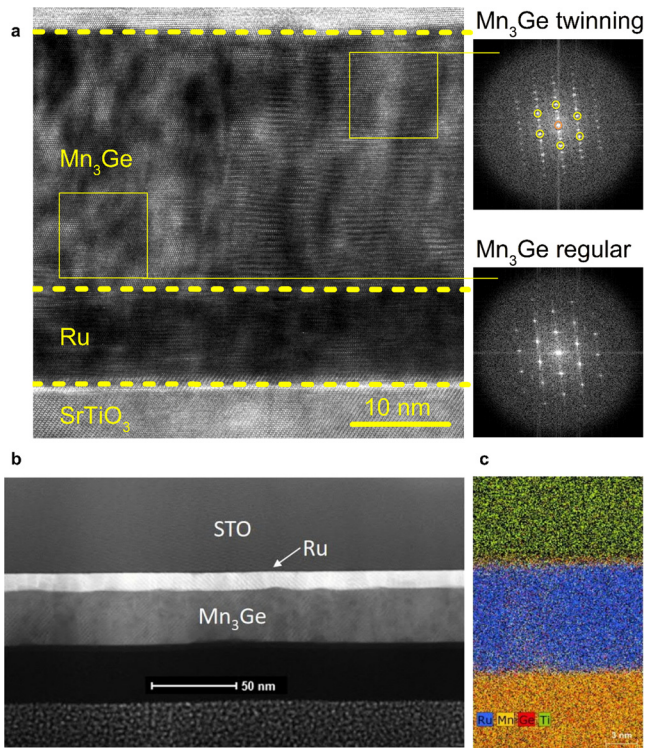

FIG. 2. Cross section TEM of a STO (111)/Ru (10 nm)/Mn_3Ge (30 nm) sample. (a) HRTEM image with insets showing FFTs of regular and twinned regions, taken from areas marked by yellow boxes. (b) HAADF-STEM image over a broader region of the film. (c) EDXS elemental mapping of Ru (blue), Mn (orange), Ge (red), and Ti (green) within part of the area imaged in (b).

Figure 2(b) depicts a cross section HAADF-STEM image of an extended area, where the substrate, Ru underlayer, and *c*-Mn_3Ge film are revealed with different contrasts. The Ru underlayer and *c*-Mn_3Ge film are both continuous with uniform thickness, sharp interfaces, and structural homogeneity. Figure 2(c) shows the corresponding EDXS elemental mapping of the stack. Mn and Ge were detected in exactly the same sample regions, therefore confirming the chemical homogeneity of the *c*-Mn_3Ge film. The clear interface between Ru and Mn demonstrates an absence of intermixing between the *c*-Mn_3Ge film and the Ru underlayer.

Having confirmed experimentally the formation of *c*-Mn_3Ge, we evaluate the stability of this nonequilibrium cubic phase compared to the well-known tetragonal and hexagonal phases by using numerical calculations to determine the structural energy of the space groups $Pm\bar{3}m$ (No. 221), $P6_3/mmc$ (No. 194), and $I4/mmm$ (No. 139). Specific details of the computational methods are given in the supplementary material. We plot the energy (E) of the three structures as a function of unit cell volume at zero temperature (T) in Fig. 3(a). While the tetragonal unit cell shows the lowest total energy, the cubic structure is lower in energy than the hexagonal phase by approximately 30 meV/unit cell. Therefore, since in our multilayer the *h*-Ru buffer layer will unfavorably seed tetragonal growth, the cubic phase of Mn_3Ge is preferred.

These calculations yield a lattice constant of 3.72 Å for the *c*-Mn_3Ge unit cell. The thermal expansion of similar noncollinear cubic materials[19] between $T = 0$ and 300 K is 0.6%. This yields a theoretical lattice constant of 3.74 Å at room temperature, which agrees with the experimentally determined value to within error and is used for further calculations.

Having confirmed the stability of the cubic crystal phase, we calculate a suggested magnetic structure for *c*-Mn_3Ge (at $T = 0$). Figure 3(b) shows the distance (d) dependent exchange parameters (J_{ij}) for *c*-Mn_3Ge. The blue curve shows exchange interactions between atoms on the inequivalent basis sites within a unit cell (nearest neighbor, NN), whereas the green curve shows exchange interactions between equivalent basis sites in different unit cells (second-NN).

At the experimentally determined lattice spacing, the NN interaction has a large, negative exchange energy of −120 meV/pair. This favors intra-plane AF coupling that, for the three Mn moments in the (111) plane of each unit cell, yields a geometrically frustrated spin texture. However, the second-NN has a smaller, positive exchange energy of 30 meV/pair. While this favors inter-plane FM coupling, the inter-plane exchange interactions are not strong enough to pull Mn moments out of the (111) planes.

Given these exchange interaction strengths, we can calculate the exchange energy resulting from different intra- (blue bonds) and inter-plane (green bonds) orientations of Mn moments in a series of candidate magnetic structures, shown in Fig. 3(c). In order of decreasing total exchange energy (with respect to the lowest energy configuration, ΔE), these proposed magnetic configurations are: purely FM order,

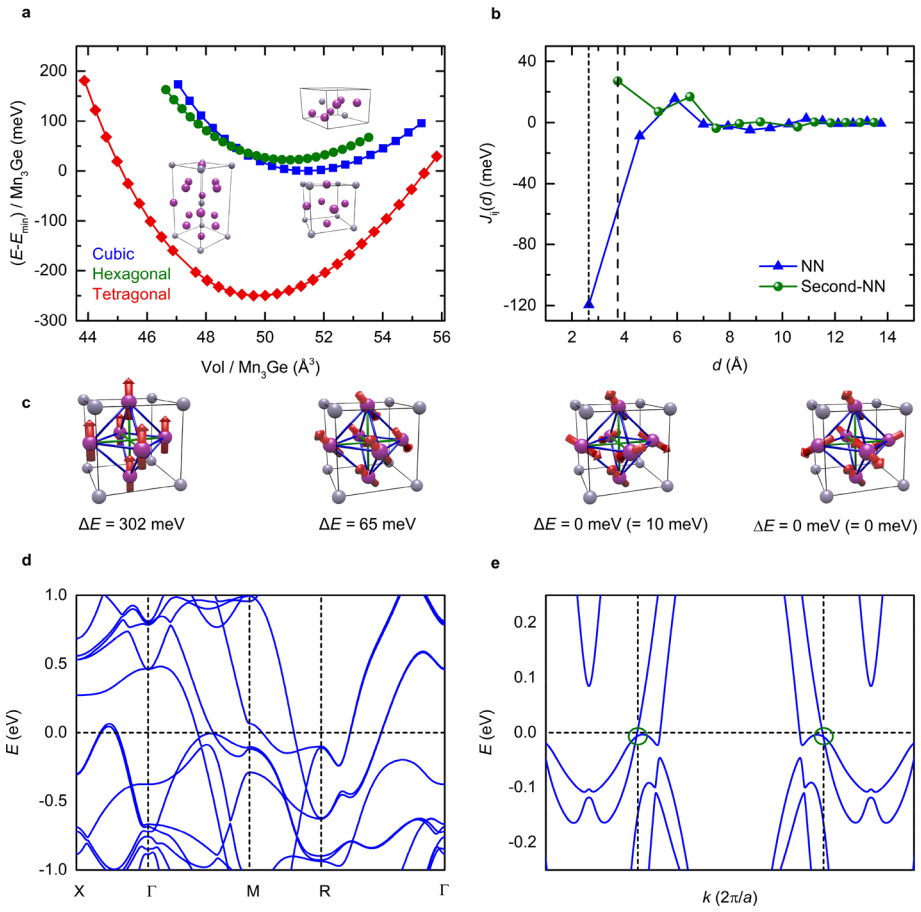

FIG. 3. (a) Energy per unit cell as a function of volume for the tetragonal unit cell (red diamonds), the hexagonal unit cell (green circles), and the cubic unit cell (blue squares). Insets illustrate the tetragonal, hexagonal, and cubic crystal structures, where purple and white spheres are the Mn and Ge atoms, respectively. (b) Exchange energy per pair in the cubic unit cell as a function of interatomic distance, considering NN (blue triangles) and second-NN (green spheres) exchange interactions. The dotted (dashed) line indicates the experimentally determined intra- (inter-) plane spacing. (c) Possible magnetic structures of *c*-Mn_3Ge with different NN (blue bonds) and second-NN (green bonds) coupling orientations; based on these, the total exchange energy for each magnetic order is calculated in comparison to the triangular AF spin texture without (with) SOC. (d) Electronic band structure along high symmetry lines in the Brillouin zone for *c*-Mn_3Ge with the all-in/all-out chiral spin texture. (e) Energy dispersion along a reciprocal space path that connects the two Weyl points (green circles), related to one another by inversion symmetry in the (111) mirror plane.

FM planes that couple AF along the [111] direction, geometrically-frustrated AF structure in the (111) planes with negative vector spin chirality, and with positive vector spin chirality. While the latter two magnetic configurations have the same energy without SOC, introducing SOC lifts this degeneracy. As such, we predict that the chiral all-in/all-out triangular spin texture is energetically favorable for *c*-Mn_3Ge.

Having determined the preferred magnetic structure for *c*-Mn_3Ge, we calculate the corresponding electronic band structure [Fig. 3(d)]. The bands around the Fermi level are dominated by Mn-*d* orbitals, which hybridize with the SOC of the Ge atoms to produce a finite momentum-space Berry curvature. There are three band anti-crossings near the Fermi level in the Γ-*M* direction. Evaluation of the bandgap and Berry curvature distribution reveal the existence of two type-II Weyl points near the Fermi level at $\pm(0.331\,28,\ 0.331\,07,\ -0.012\,16)(2\pi/a)$ in the Brillouin zone, shown in Fig. 3(e). The corresponding pair of Weyl points acts as the source and sink of Berry curvature, expected to generate strong AHE and SHE responses.

Within this chiral spin texture, an antisymmetry operation can be applied to create two magnetic structures, with opposite handedness of the all-in/all-out noncollinear order. Because these are degenerate, even in the presence of SOC, we expect *c*-Mn_3Ge to form two types of AF domains, similar to *c*-Mn_3Ir.[14] These two chiral senses of rotation generate opposite AHE but the same SHE,[15] arising from the Berry curvature of the electronic structure.

The potential for *c*-Mn_3Ge to host noncollinear antiferromagnetism makes these films of interest for topological spin-orbitronics. This motivates us to study the films' magnetic and transport properties. Magnetization was measured using a Quantum Design MPMS3 vibrating sample magnetometer. The *c*-Mn_3Ge films show no net moment (m) when we apply external magnetic field ($\mu_0 H$) either in-plane (IP) or out-of-plane (OP) [Fig. 4(a)]. We, therefore, rule out the possible ferromagnetic ordering previously suggested for the cubic phase of bulk crystals.[18] Instead, the absence of magnetization supports the assertion that *c*-Mn_3Ge is antiferromagnetic.

To elucidate explicitly the AF properties of the *c*-Mn_3Ge phase, we study exchange bias (EB) in *c*-Mn_3Ge/Py bilayers. EB occurs because of uncompensated moments in the AF at the interface.[20] These arise from imperfections in the AF structure at the edges of crystalline grains and exchange couple both to the bulk AF domain structure as well as to the FM layer.[21] Above the so-called blocking temperature (T_B) of the bilayer, these uncompensated moments follow the magnetization of the FM and hence can be manipulated using an external magnetic field. As the bilayer is cooled through T_B, the AF domain structure becomes pinned, thus fixing the direction of the interfacial moments. This introduces a unidirectional anisotropy to the magnetization of the FM layer.[22]

EB in *c*-Mn_3Ge is demonstrated in the inset of Fig. 4(a). This summarizes the magnetization (M) hysteresis loops for a *c*-Mn_3Ge

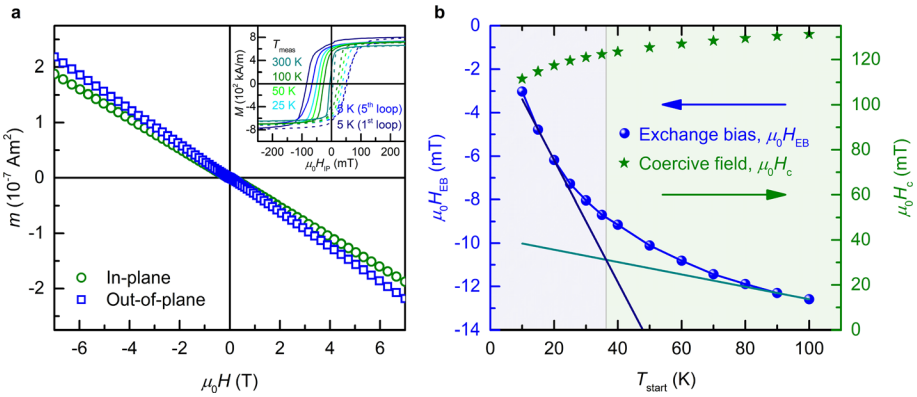

FIG. 4. (a) Magnetic moment measured at 300 K for a 40 nm *c*-Mn_3Ge film as a function of magnetic field applied IP along the [1 $\bar{1}$ 0] direction and OP along the [111] direction. Inset shows normalized magnetization hysteresis loops of a *c*-Mn_3Ge (40 nm)/Py (5 nm) bilayer, measured after cooling from 350 to 5 K in a 1-T IP magnetic field, then warming to different measurement temperatures, T_{meas}. At base temperature, loops measured both directly after cooling and following five field cycles are shown. b) Exchange bias (blue spheres) and coercive (green stars) fields extracted from hysteresis loops measured at 5 K, following cooling in a 1-T IP magnetic field from different starting temperatures, T_{start} (x axis). As T_{start} approaches the blocking temperature, T_B, from above, the exchange bias field will decrease; linear fits to this curve, where $T_{start} > T_B$ (green) and $T_{start} < T_B$ (blue), yield an estimate of T_B at their intercepts (indicated by shaded regions).

(40 nm)/Py (5 nm) bilayer. We measured these after field cooling to 5 K under a 1-T IP magnetic field, cycling the externally applied field five times, and then warming to progressively higher measurement temperatures (T_{meas}). A detailed description of the exchange bias measurement protocol is given in the supplementary material. A shift of the hysteresis loop, the so-called exchange bias field ($\mu_0 H_{EB}$), and a broadening of the coercive field ($\mu_0 H_c$), which increase at lower T_{meas}, point to the initiation of unidirectional anisotropy in the Py layer.

In order to identify T_B, we subsequently demagnetized the bilayer at 350 K, cooled under a zero applied field to progressively decreasing starting temperatures (T_{start}), then cooled under a 1-T IP magnetic field to 5 K. Here, we measured hysteresis loops, with the extracted $\mu_0 H_{EB}$ and $\mu_0 H_c$ plotted as a function of T_{start} in Fig. 4(b). To determine T_B, we perform linear fits in the higher temperature and lower temperature regions of the curve. The intercept of these linear fits allows us to estimate $T_B \sim 35$ K for this EB system.

The magnitude of the EB fields achieved in *c*-Mn_3Ge (up to $\mu_0 H_{EB} = 16$ mT at 5 K on the initial loop) are comparable with other cubic or hexagonal AFs[23] including the disordered cubic Mn_3Ge phase.[17] Thus, the presence of EB suggests long-range AF ordering and, since particularly strong EB effects are found in noncollinear AFs,[16] provides evidence for a similar spin texture in our *c*-Mn_3Ge films. EB was also measured in a *c*-Mn_3Ge (10 nm)/Py (5 nm) bilayer (see supplementary material Fig. S5).

Finally, we investigated the magnetotransport of the *c*-Mn_3Ge films, in lithographically patterned devices. Details of the fabrication, measurement, and analysis procedures, as well as longitudinal resistivity measurements at low temperature, are given in the supplementary material.

Transverse resistivity (ρ_{xy}) as a function of the OP magnetic field is shown in Fig. 5. *c*-Mn_3Ge displays an ordinary Hall effect, similar to other cubic noncollinear AFs such as Mn_3Ir.[14] The absence of AHE suggests the presence of multiple AF domains with opposite chiral sense-of-rotation. These correspond to the two degenerate all-in/all-out spin texture configurations predicted by first-principles calculations. A preferential domain orientation cannot be achieved using a magnetic field because of the absence of a net magnetic moment, which is prohibited by the strong MCA in the $L1_2$-type structure.

Fitting to the experimental data yields a negative Hall coefficient of 1.7×10^{-2} $\mu\Omega$ cm T^{-1}. Using a one-carrier model, we calculate an electron-type charge carrier concentration of 3.6×10^{22} cm^{-3} for a representative 40-nm-thick *c*-Mn_3Ge film at 300 K. This value compares with the theoretical calculated carrier concentration of 6.4×10^{22} cm^{-3} at the Fermi energy, an estimate that includes all charge carriers.

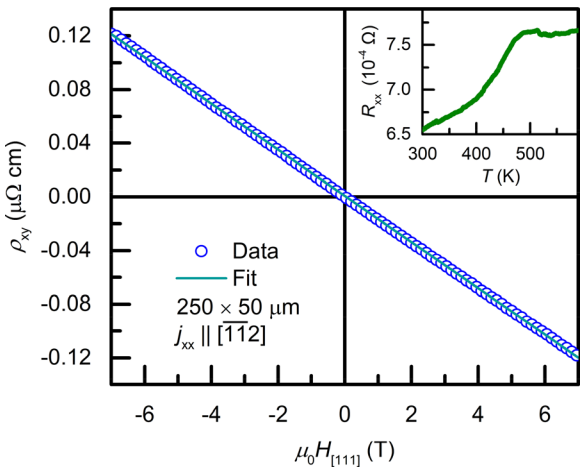

FIG. 5. Transverse resistivity measured at 300 K for a 40 nm *c*-Mn_3Ge film patterned into a 250 × 50 μm^2 Hall bar as a function of magnetic field applied OP along the [111] direction, with current (j_{xx}) flowing along the [$\bar{1}$12] direction and the underlayer contribution subtracted. Inset shows longitudinal resistance measured on heating above room temperature in an inert atmosphere for an unpatterned 10 nm *c*-Mn_3Ge film.

Because the absence of net moment makes determining the Néel temperature (T_N) of c-Mn_3Ge using magnetometry challenging, we measured longitudinal resistance (R_{xx}) as a function of temperature above 300 K (inset to Fig. 5). At ≈490 K, a broad change of slope occurs, driven by s-d band scattering of conduction electrons. The steeper slope of $R_{xx}(T)$ below 490 K is because of increasing spin disorder scattering when approaching the magnetic ordering temperature from below. We thus conclude that the film shows a long-range magnetic order transition around 490 ± 10 K, allowing us to place T_N of the c-Mn_3Ge films in this range.

Therefore, the chiral all-in/all-out spin texture is stable at room temperature, making c-Mn_3Ge of interest for potential topological spintronic applications. Furthermore, AF/FM heterostructures of the type studied here will facilitate the construction of spintronic devices containing c-Mn_3Ge, such as tunneling anisotropic magnetoresistance junctions[24] or components for the field-free spin–orbit torque switching of an exchange-biased FM layer using spin current generated in the AF.[25]

Such spin currents can arise as a result of the chiral spin texture[26] that we predict for ordered c-Mn_3Ge. While we find similar physical properties to those reported by Koyabashi *et al.*,[17] the $L1_2$ ordering found in our c-Mn_3Ge films may yield additional applications in topological spin-orbitronic devices. Future work should investigate spin transport properties in c-Mn_3Ge showing chiral noncollinear antiferromagnetism.

In conclusion, we have grown heteroepitaxial (111)-oriented cubic Mn_3Ge thin films with an $L1_2$-type structure. The c-Mn_3Ge films show no net magnetization, attributed to their antiferromagnetism, and no anomalous Hall effect, attributed to multiple domains of opposite chirality. When coupled to a ferromagnet, c-Mn_3Ge induces unidirectional anisotropy, confirming an antiferromagnetic ordering. We show, from first-principles calculations, that this is likely a noncollinear all-in/all-out magnetic structure, with simulation of the corresponding band structure revealing Weyl points. These epitaxial thin films of c-Mn_3Ge with chiral spin texture could, therefore, serve as a material for spin current generation in topological spin-orbitronic devices.

See the supplementary material for details on thin film deposition recipes, extended x-ray diffraction characterization, computational methods, magnetic and transport measurement procedures, exchange bias results for a thinner 10 nm c-Mn_3Ge/5 nm Py bilayer, and electrical transport measurements at low temperature.

We thank Georg Woltersdorf for helpful discussions. The authors acknowledge the EU FET Open RIA Grant No. 766566 (ASPIN) and the European Union's Horizon 2020 research and innovation program, under FET-Proactive Grant Agreement No. 824123 (SKYTOP). J.M.T. acknowledges funding from the Deutsche Forschungsgemeinschaft under Project-ID 328545488 (TRR 227, project B10). J.G. acknowledges support from the Air Force Office of Scientific Research (under Award No. FA9550-23-1-0132) and the Max Planck Society through the Max Planck Partner Group Program. D.K. acknowledges the Ministry of Education of the Czech Republic (Grant Nos. LM2018110 and LNSM-LNSpin), the Czech Academy of Sciences (Project No. LQ100102201), and the Czech Science Foundation (Grant No. 22-22000M).

AUTHOR DECLARATIONS

Conflict of Interest

The authors have no conflicts to disclose.

Author Contributions

Anastasios Markou and James M. Taylor contributed equally to this work.

Anastasios Markou: Investigation (equal); Project administration (equal); Visualization (equal); Writing – original draft (equal). **Claudia Felser:** Conceptualization (equal); Funding acquisition (equal); Supervision (equal); Writing – review & editing (equal). **Stuart S.P. Parkin:** Conceptualization (equal); Funding acquisition (equal); Supervision (equal); Writing – review & editing (equal). **James Mark Taylor:** Investigation (equal); Visualization (equal); Writing – original draft (equal). **Jacob Gayles:** Formal analysis (equal); Software (equal); Visualization (equal). **Yan Sun:** Formal analysis (equal); Software (equal); Visualization (equal). **Dominik Kriegner:** Investigation (equal); Visualization (equal). **Joerg Grenzer:** Investigation (equal); Resources (equal). **Shanshan Guo:** Investigation (equal). **Walter Schnelle:** Investigation (equal); Methodology (equal). **Edouard Lesne:** Investigation (equal); Writing – review & editing (equal).

DATA AVAILABILITY

The data that support the findings of this study are available from the corresponding authors upon reasonable request.

REFERENCES

[1]L. Šmejkal, Y. Mokrousov, B. Yan, and A. H. MacDonald, Nat. Phys. **14**(3), 242 (2018).
[2]N. Nagaosa, J. Sinova, S. Onoda, A. H. MacDonald, and N. P. Ong, Rev. Mod. Phys. **82**(2), 1539 (2010).
[3]J. Sinova, S. O. Valenzuela, J. Wunderlich, C. H. Back, and T. Jungwirth, Rev. Mod. Phys. **87**(4), 1213 (2015).
[4]B. Göbel, I. Mertig, and O. A. Tretiakov, Phys. Rep. **895**, 1 (2021).
[5]J. Sticht, K. H. Höck, and J. Kübler, J. Phys.: Condens. Matter **1**(43), 8155 (1989).
[6]L. Šmejkal, A. H. MacDonald, J. Sinova, S. Nakatsuji, and T. Jungwirth, Nat. Rev. Mater. **7**(6), 482 (2022).
[7]J. Jeong, Y. Ferrante, S. V. Faleev, M. G. Samant, C. Felser, and S. S. P. Parkin, Nat. Commun. **7**(1), 10276 (2016).
[8]S. Tomiyoshi, Y. Yamaguchi, and T. Nagamiya, J. Magn. Magn. Mater. **31–34**, 629 (1983).
[9]A. Kalache, G. Kreiner, S. Ouardi, S. Selle, C. Patzig, T. Höche, and C. Felser, APL Mater. **4**(8), 086113 (2016).
[10]A. K. Nayak, J. E. Fischer, Y. Sun, B. Yan, J. Karel, A. C. Komarek, C. Shekhar, N. Kumar, W. Schnelle, J. Kübler, C. Felser, and S. S. P. Parkin, Sci. Adv. **2**(4), e1501870 (2016).
[11]T. Higo, H. Man, D. B. Gopman, L. Wu, T. Koretsune, O. M. J. van 't Erve, Y. P. Kabanov, D. Rees, Y. Li, M. T. Suzuki, S. Patankar, M. Ikhlas, C. L. Chien, R. Arita, R. D. Shull, J. Orenstein, and S. Nakatsuji, Nat. Photonics **12**(2), 73 (2018).
[12]K.-R. Jeon, B. K. Hazra, K. Cho, A. Chakraborty, J.-C. Jeon, H. Han, H. L. Meyerheim, T. Kontos, and S. S. P. Parkin, Nat. Mater. **20**(10), 1358 (2021).
[13]H. Chen, Q. Niu, and A. H. MacDonald, Phys. Rev. Lett. **112**(1), 017205 (2014).
[14]J. M. Taylor, E. Lesne, A. Markou, F. K. Dejene, P. K. Sivakumar, S. Pöllath, K. Gaurav Rana, N. Kumar, C. Luo, H. Ryll, F. Radu, F. Kronast, P. Werner, C. H. Back, C. Felser, and S. S. P. Parkin, Appl. Phys. Lett. **115**(6), 062403 (2019).
[15]W. Zhang, W. Han, S. H. Yang, Y. Sun, Y. Zhang, B. Yan, and S. S. P. Parkin, Sci. Adv. **2**(9), e1600759 (2016).

[16]J. M. Taylor, E. Lesne, A. Markou, F. K. Dejene, B. Ernst, A. Kalache, K. Gaurav Rana, N. Kumar, P. Werner, C. Felser, and S. S. P. Parkin, Phys. Rev. Mater. **3**(7), 074409 (2019).
[17]A. Kobayashi, T. Higo, S. Nakatsuji, and Y. Otani, AIP Adv. **10**(1), 015225 (2020).
[18]H. Takizawa, T. Yamashita, K. Uheda, and T. Endo, J. Phys.: Condens. Matter **14**(44), 11147 (2002).
[19]K. Fukamichi, R. Y. Umetsu, A. Sakuma, and C. Mitsumata, in *Handbook of Magnetic Materials*, edited by K. H. J. Buschow (Elsevier, 2006), Vol. 16, p. 209.
[20]A. P. Malozemoff, Phys. Rev. B **35**(7), 3679 (1987).
[21]A. P. Malozemoff, J. Appl. Phys. **63**(8), 3874 (1988).
[22]J. Nogués and I. K. Schuller, J. Magn. Magn. Mater. **192**(2), 203 (1999).
[23]H.-C. Wu, Z.-M. Liao, R. G. Sumesh Sofin, G. Feng, X.-M. Ma, A. B. Shick, O. N. Mryasov, and I. V. Shvets, Adv. Mater. **24**(47), 6374 (2012).
[24]B. G. Park, J. Wunderlich, X. Martí, V. Holý, Y. Kurosaki, M. Yamada, H. Yamamoto, A. Nishide, J. Hayakawa, H. Takahashi, A. B. Shick, and T. Jungwirth, Nat. Mater. **10**(5), 347 (2011).
[25]J. Železný, P. Wadley, K. Olejník, A. Hoffmann, and H. Ohno, Nat. Phys. **14**(3), 220 (2018).
[26]B. K. Hazra, B. Pal, J.-C. Jeon, R. R. Neumann, B. Göbel, B. Grover, H. Deniz, A. Styervoyedov, H. Meyerheim, I. Mertig, S.-H. Yang, and S. S. P. Parkin, Nat. Commun. **14**(1), 4549 (2023).